NUMERICAL SIMULATIONS OF RESONANT OSCILLATIONS IN A TUBE

Hua-Zhong Tang and Ping Cheng

Department of Mechanical Engineering, The Hong Kong University of Science and Technology, Clear Water Bay, Kowloon, Hong Kong

Kun Xu

Department of Mathematics, The Hong Kong University of Science and Technology, Clear Water Bay, Kowloon, Hong Kong

The article concerns a genuinely two-dimensional numerical study of resonant oscillation phenomena in a gas-filled tube with an isothermal wall or an adiabatic wall. The time-dependent, axisymmetric, compressible Navier–Stokes equations in two dimensions are solved by a new finite volume method with the second-order kinetic flux-vector splitting (KFVS) scheme for convective terms, and a third-order Runge–Kutta method for the time evolution. The oscillatory motion of the fluid in a closed tube is generated by a piston at one end, and reflected by the other closed end. Weak shock waves propagating within the tube at the resonant frequency and slightly off-resonance frequencies are numerically captured, which are consistent with both experimental observation and previous theoretical analyses. The interesting results of the sudden change in axial velocity near the piston and the closed end are also presented.

INTRODUCTION

The understanding of gas oscillating behavior inside a tube is of both fundamental and practical interest [1–11]. Saenger and Hudson [1] observed from experiments that a weak shock wave would appear in a closed tube if a piston was oscillating at the resonant frequency on the other end of the tube. To explain this observation, Saenger and Hudson [1] tried to construct theoretical models based on the existence of propagating shock waves. However, their analysis was not very successful because viscosity and heat conduction were not taken into consideration, and the amplitude of gas oscillation became infinite. Later, Betchov [2] showed that nonlinear cumulative effects could lead to finite amplitude gas oscillations in a closed tube even if viscosity and heat conduction were not considered. By combining the

NOMENCLATURE

$A_{i,j}$	control volume	R_0	radius of tube
C_p	specific heat at constant pressure	T	temperature
e	total energy	u	axial velocity
E, F	convective fluxes	U	conservative variables
$\dot{E}, \dot{F}$	diffusive fluxes	$(\tilde{u}, \tilde{v})$	molecular velocity
g	Maxwell–Boltzmann distribution	v	radial velocity
		ρ	density
k	thermal conductivity coefficient	μ	viscosity
K	internal degree of freedom	τ	stress tensor
L	length of tube	Ψ	moment function vector
M	number of grid points in axial direction	γ	ratio of the specific heats
		Δt	grid size in time t direction
N	number of grid points in radial direction	Δx	grid size in axial direction
		Δr	grid size in radial direction
p	pressure	ξ	internal particle velocity
Pr	Prandtl number		

method of characteristics and a perturbation method with both gas compressibility and viscosity taken into consideration, Chester [3] was able to predict the shape and strength of the shock waves. Most recently, a number of perturbation solutions have been published on thermoacoustic effects in a resonant tube with applications to thermoacoustic machine. (See [4–7] and the references therein.)

Although there exist a few numerical investigations of wave propagation in a tube [8–9], they are restricted to solving one-dimensional nonlinear Lagrangian wave equations. As far as the authors are aware, a numerical simulation of resonant oscillations of a two-dimensional compressible viscous flow inside a closed tube and its subsequent appearance of shock waves has not been carried out. There exist several difficulties in the numerical simulation of such a compressible flow by solving fully compressible Navier–Stokes equations. First, the appearance of weak shock waves in resonant oscillations requires a high-resolution numerical scheme so that discontinuities can be captured sharply. Thus, application of some high-order schemes (such as MacCormack's scheme and the Lax–Wendroff scheme) to the current problem would lead to numerical oscillations. Second, the extremely small Mach number of the gas flow in the tube would result in small spatial pressure variations but affect the velocity field at leading order [10]. The third difficulty is that it would require a great deal of computer time before the appearance of shock waves in the simulation, thus requiring a highly accurate numerical scheme in time so that numerical dissipation because of truncation errors would not lead to inaccurate numerical results.

During the last two decades, various high-resolution schemes for capturing discontinuous solutions have been developed for the Euler equations [11–13] as well as for the Navier–Stokes equations [14,15]. These include total variation diminishing (TVD) schemes [11] and essentially nonoscillation (ENO) schemes [12], and so on. In the development of modern high-resolution shock capturing methods, the Monotone Upstream-Centered Schemes for Conservation Laws (MUSCL) interpolation tech-

nique [13] has played an important role. We refer the readers to [16, 17] and the references therein for a detailed introduction to high-resolution methods. The main features of a high-resolution scheme include the following:

- at least second-order accuracy for smooth solutions,
- sharp resolution of discontinuities without excess smearing, and
- the absence of spurious oscillations in the computed solution.

To capture accurate discontinuity solutions in aerodynamic applications, most high-resolution methods have intrinsically implemented approximate or exact Riemann solvers. This requires considerable work and cost for the simulation of any physical problems. Because of this, the flux-vector splitting methods and other high-resolution shock capturing methods without implementation of Rieman solvers, such as gas-kinetic methods, have been developed in recent years [18–21].

In this article, first we use a high-resolution shock-capturing scheme for the unsteady axisymmetric compressible Navier–Stokes equations to simulate numerically resonant oscillation phenomena in a gas-filled tube with an isothermal wall or an adiabatic wall. In the construction of the current scheme, the kinetic flux-vector splitting and and the initial reconstruction technique [13] are used for the convective terms, second-order central difference for derivatives in the diffusive terms, and the source terms. For time evolution, we use a third-order Runge–Kutta method to relax the time constraints.

GOVERNING EQUATIONS

Let x and r denote the axial and radial coordinates; t is the time; u and v denote the velocity components in x- and r-directions, respectively; and ρ, e, and p denote the fluid density, the total energy per unit volume, and the pressure, respectively. The axisymmetric Navier–Stokes equations for a compressible fluid can be written in the following conservative form:

$$\frac{\partial r\,U}{\partial t} + \frac{\partial r(E - \tilde{E})}{\partial x} + \frac{\partial r(F - \tilde{F})}{\partial r} = S(U) \qquad (1)$$

where the conservative variables U, the source term $S(U)$, convective fluxes E and F, and the diffusive fluxes $\tilde{E}$ and $\tilde{F}$, are defined by

$$U = [\rho, \rho u, \rho v, e]^T$$

$$S(U) = [0, 0, p - \tau_{\theta\theta}, 0]^T$$

$$E(U) = [\rho u, \rho u^2 + p, \rho uv, u(e + p)]^T$$

$$\tilde{E}(U) = \left[0, \tau_{xx}, \tau_{xr}, u\tau_{xx} + v\tau_{xr} + k\frac{\partial T}{\partial x}\right]^T$$

$$F(U) = [\rho v, \rho uv, \rho v^2 + p, v(e + p)]^T$$

$$\tilde{F}(U) = \left[0, \tau_{rx}, \tau_{rr}, u\tau_{rx} + v\tau_{rr} + k\frac{\partial T}{\partial r}\right]^T \qquad (2)$$

In Eq. (2), τ_{xx}, τ_{xr}, and τ_{rr} denote the components of the stress tensor given by

$$\tau_{xx} = (2\mu + \tilde{\mu})\frac{\partial u}{\partial x} + \tilde{\mu}\left(\frac{v}{r} + \frac{\partial v}{\partial r}\right)$$

$$\tau_{rr} = (2\mu + \tilde{\mu})\frac{\partial v}{\partial r} + \tilde{\mu}\left(\frac{v}{r} + \frac{\partial u}{\partial x}\right)$$

$$\tau_{\theta\theta} = (2\mu + \tilde{\mu})\frac{v}{r} + \tilde{\mu}\left(\frac{\partial v}{\partial r} + \frac{\partial u}{\partial x}\right)$$

$$\tau_{xr} = \tau_{rx} = \mu\left(\frac{\partial u}{\partial r} + \frac{\partial v}{\partial x}\right) \tag{3}$$

Here $\tilde{\mu} = -2/3\mu$, and μ and k denote the viscosity and the thermal conductivity coefficients, respectively, and T is the gas temperature. The viscosity of the fluid is defined by Sutherland's law

$$\mu = \mu_0\left(\frac{T}{T_0}\right)^{1.5}\frac{T_0 + C}{T + C} \tag{4}$$

where T_0 and μ_0 are reference values at standard sea level conditions, and C is a given constant that is equal to 110. If the Prandtl number is assumed to be constant (approximately equal to 0.71 for calorically perfect air), thermal conductivity can be calculated from the equation $\text{Pr} = \mu C_p/k$, where C_p is the specific heat at constant pressure.

For a perfect gas, the pressure is related to the total energy e by

$$p = (\gamma - 1)[e - \tfrac{1}{2}\rho(u^2 + v^2)]$$

NUMERICAL METHODS

Space Discretizations

Let $x_i = i\Delta x$ and $r_j = j\Delta r$ ($i = 0, 1, \ldots, M; j = 0, 1, \ldots, N$) denote grid points in x- and r-directions, respectively, where $\Delta x = L/M$ and $\Delta r = R_0/N$; then the computational domain $[0, L] \times [0, R_0]$ is subdivided into quadrilaterals as shown in Figure 1.

Integrating Eq. (1) over a control volume $A_{i,j} = [x_{i-1/2}, x_{i+1/2}] \times [r_{j-1/2}, r_{j+1/2}]$ gives

$$\frac{\partial}{\partial t}\iint_{A_{i,j}} rU \, dx \, dr + \int_{r_{j-1/2}}^{r_{j+1/2}} r((E - \tilde{E})_{i+1/2} - (E - \tilde{E})_{i-1/2}) \, dr$$

$$+ \int_{x_{i-1/2}}^{x_{i+1/2}} (r_{j+1/2}(F - \tilde{F})_{j+1/2} - r_{j-1/2}(F - \tilde{F})_{j-1/2}) \, dx$$

$$= \iint_{A_{i,j}} S(U) \, dx \, dr$$
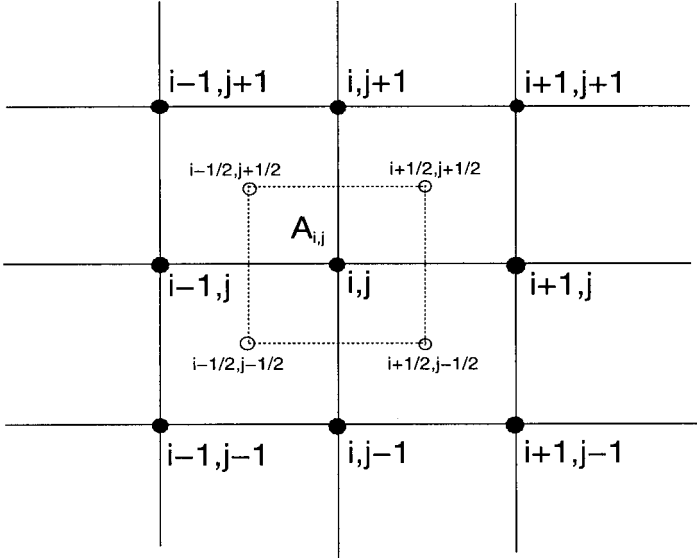
Figure 1. Grid points (●) and control volume $A_{i,j}$ surrounded by the dashed lines.

which can be approximated using a midpoint formula such as

$$\frac{\partial}{\partial t} r_j U_{i,j}(t) + \frac{r_j}{\Delta x}[(E - \tilde{E})_{i+1/2,j} - (E - \tilde{E})_{i-1,2,j}]$$

$$+ \frac{1}{\Delta r}[r_{j+1/2}(F - \tilde{F})_{i,j+1/2} - r_{j-1/2}(F - \tilde{F})_{i,j-1/2}]$$

$$= \frac{1}{\Delta x \Delta r} \iint_{A_{i,j}} S(U)\, dx\, dr \tag{5}$$

where $U_{i,j}(t)$ denote the cell averaged conservative variables defined by

$$U_{i,j}(t) = \frac{1}{\Delta x \Delta r} \int_{x_{i-1/2}}^{x_{i+1/2}} \int_{r_{j-1/2}}^{r_{j+1/2}} U(x, r, t)\, dx\, dr$$

?twb=.60w›The approximation given by Eq. (5) keeps second-order accuracy in space. Based on the conservative variables at the cell center, the convective and diffusive fluxes across cell interfaces have to be evaluated according to the gas evolution models.

In the following we are going to construct the convective fluxes across each cell interface of the control volume $A_{i,j}$. Following the collisionless gas evolution model [21], the macroscopic fluxes $E(U)$ and $F(U)$ can be split into two parts, that is, positive and negative fluxes

$$E(U) = E(U)^+ + E(U)^- \qquad F(U) = F(U)^+ + F(U)^- \tag{6}$$

where $E^\pm$ and $F^\pm$ are given by

$$E^{\pm}(U) = \langle \Psi, \tilde{u}g \rangle_{\pm} \equiv \pm \int_{R^{K+1}} \int_{0}^{\pm\infty} \tilde{u}\Psi g \, d\tilde{u} \, d\tilde{v} \, d\xi$$

$$F^{\pm}(U) = \langle \Psi, \tilde{v}g \rangle_{\pm} \equiv \pm \int_{R^{K+1}} \int_{0}^{\pm\infty} \tilde{v}\Psi g \, d\tilde{v} \, d\tilde{u} \, d\xi \tag{7}$$

In Eq. (7), $R = (-\infty, \infty)$, $(\tilde{u}, \tilde{v})$ denote molecular velocity components in x- and r-directions; $d\xi = \xi_1, \ldots, d\xi_K$ and $\xi_1, \ldots, \xi_K$ are the components of the internal particle velocity in K dimension space. For the flow movement in the two-dimensional case, K is related to the ratio of specific heat γ through the relation $K = (3 - \gamma)/(\gamma - 1) - 1$. Here g is the Maxwell–Boltzmann distribution for the equilibrium state

$$g = \rho \left(\frac{\lambda}{\pi} \right)^{(K+2)/2} e^{-\lambda[(\tilde{u}-u)^2 + (\tilde{v}-v)^2 + \xi^2]} \tag{8}$$

and Ψ is the moment function vector

$$\Psi = \left[1, \tilde{u}, \tilde{v}, \frac{\tilde{u}^2 + \tilde{v}^2 + \xi^2}{2} \right]^T \tag{9}$$

where $\xi^2 = \xi_1^2 + \cdots + \xi_K^2$, and λ is a function of temperature such that $\lambda = \rho/2p$. The splitting fluxes $E^{\pm}$ and $E^{\pm}$ have the explicit forms

$$E^{\pm}(U) = \begin{pmatrix} \rho\langle\tilde{u}\rangle_{\pm} \\ \rho\langle\tilde{u}^2\rangle_{\pm} \\ \rho\langle\tilde{u}\rangle_{\pm}\langle\tilde{v}\rangle \\ \frac{1}{2}\rho(\langle\tilde{u}^3\rangle_{\pm} + \langle\tilde{u}\rangle_{\pm}(\langle\tilde{v}^2\rangle + \langle\xi^2\rangle)) \end{pmatrix} \tag{10}$$

and

$$F^{\pm}(U) = \begin{pmatrix} \rho\langle\tilde{v}\rangle_{\pm} \\ \rho\langle\tilde{v}\rangle_{\pm}\langle\tilde{u}\rangle \\ \rho\langle\tilde{v}^2\rangle_{\pm} \\ \frac{1}{2}\rho(\langle\tilde{v}^3\rangle_{\pm} + \langle\tilde{v}\rangle_{\pm}(\langle\tilde{u}^2\rangle + \langle\xi^2\rangle)) \end{pmatrix} \tag{11}$$

where

$$\langle\xi^2\rangle = \frac{K}{2\lambda}$$

$$\langle\tilde{u}\rangle = u \qquad \langle\tilde{u}^2\rangle = u^2 + \frac{1}{2\lambda}$$

$$\langle\tilde{u}^0\rangle_{\pm} = \frac{1}{2} \, \text{erfc}(\mp\sqrt{\lambda}u)$$

$$\langle\tilde{u}\rangle_{\pm} = u\langle\tilde{u}^0\rangle_{\pm} \pm \frac{e^{-\lambda u^2}}{2\sqrt{\lambda\pi}}$$

$$\cdots\cdots$$

$$\langle \tilde{u}^{m+2} \rangle_\pm = u \langle \tilde{u}^{m+1} \rangle_\pm + \frac{m+1}{2\lambda} \langle \tilde{u}^m \rangle_\pm \qquad m = 0, 1, 2, \ldots$$

The formulas of $\langle \tilde{v}^m \rangle_\pm$ and $\langle \tilde{v}^m \rangle$ are the same as the above, with u replaced by v. Here $\mathrm{erfc}(x)$ is the complementary error function

Based on the above kinetic flux-vector splitting (KFVS) formulation (6), the convective fluxes $E(U)$ and $F(U)$ at each cell interface of the control volume $A_{i,j}$ can be obtained and Eq. (5) becomes

$$\frac{\partial}{\partial t} r_j U_{i,j}(t) + \frac{r_j}{\Delta x}[G(U_{i,j}, U_{i+1,j}) - G(U_{i-1,j}, U_{i,j})]$$

$$+ \frac{1}{\Delta r}[r_{j+1/2} H(U_{i,j}, U_{i,j+1}) - r_{j-1/2} H(U_{i,j}, U_{i,j})]$$

$$- \frac{r_j}{\Delta x}[\tilde{E}_{i+1,2,j} - \tilde{E}_{i-1,2,j}] - \frac{1}{\Delta r}[r_{j+1/2}\tilde{F}_{i,j+1/2} - r_{j-1/2}\tilde{F}_{i,j-1/2}]$$

$$= \frac{1}{\Delta x \Delta r} \iint_{A_{i,j}} S(U)\, dx\, dr \tag{12}$$

where convective fluxes $G(U_{i,j}, U_{i+1,j})$ and $H(U_{i,j}, U_{i,j+1})$ are defined as

$$G(U_{i,j}, U_{i+1,j}) = E^+(U_{i,j}) + E^-(U_{i+1,j})$$
$$H(U_{i,j}, U_{i,j+1}) = F^+(U_{i,j}) + F^-(U_{i,j+1}) \tag{13}$$

It is well known that the above finite volume scheme is only first-order accurate in space. To improve the accuracy of the scheme, the initial reconstruction technique [13] has to be applied to interpolate the cell averaged variables to the cell interfaces. For example, a linear function

$$\bar{U}_{i,j}(x, r) = U_{i,j} + (U_x)_{i,j}(x - x_i) + (U_r)_{i,j}(r - r_j)$$
$$\text{for } (x, r) \in [x_{i-1/2}, x_{i+1/2}] \times [r_{j-1/2}, r_{j+1/2}] \tag{14}$$

can be constructed to approximate the cell averaged variables $U_{i,j}$ at the beginning of each time step, where $(U_x)_{i,j}$ and $(U_r)_{i,j}$ are the approximate slopes in the x- and r-directions inside the control volume A_{ij}; that is,

$$(U_x)_{i,j} = \left(\frac{\partial U}{\partial x}\right)_{i,j} + O((\Delta x)^p) \quad (U_r)_{i,j} = \left(\frac{\partial U}{\partial r}\right)_{i,j} + O((\Delta r)^p) \quad p \geq 1$$

To avoid overshoot and undershoot in he reconstructed initial data, the slopes of U, that is $\partial U/\partial x$ and $\partial U/\partial r$, have to be limited. In this article, the van Leer limiter [13] is used; that is,

$$(U_x)_{i,j} = (\mathrm{sgn}(s_{i,j}^+) + \mathrm{sgn}(s_{i,j}^-)) \frac{|s_{i,j}^+||s_{i,j}^-|}{|s_{i,j}^+| + |s_{i,j}^-|} \tag{15}$$

where sgn is the sign function, and

$$S_{i,j}^+ = (U_{i+1,j}^n - U_{i,j}^n)/(x_{i+1,j} - x_{i,j}) \qquad s_{i,j}^- = (U_{i,j}^n - U_{i-1,j}^n)/(x_{i,j} - x_{i-1,j}) \tag{16}$$

are the corresponding slopes in the neighboring cells. Similarly, $(U_r)_{i,j}$ can be obtained.

Based on the reconstruction given in Eq. (14), we can establish a high-order spatial resolution solver for Eq. (1) as follows:

$$
\begin{aligned}
\frac{\partial}{\partial t} r_j U_{i,j}(t) = & -\frac{r_j}{\Delta x}[G(\tilde{U}_{i+1/2,j}, \hat{U}_{i+1/2,j}) - G(\hat{U}_{i-1/2,j}, \tilde{U}_{i-1/2,j})] \\
& -\frac{1}{\Delta r}[r_{j+1/2}H(\tilde{U}_{i,j+1/2}, \hat{U}_{i,j+1/2}) - r_{j-1/2}H(\tilde{U}_{i,j-1/2}, \hat{U}_{i,j-1/2})] \\
& +\frac{r_j}{\Delta x}[\tilde{E}_{i+1/2,j} + \tilde{E}_{i-1/2,j}] + \frac{1}{\Delta r}[r_{j+1/2}\tilde{F}_{i,j+1/2} - r_{j-1/2}\tilde{F}_{i,j-1/2}] \\
& +\frac{1}{\Delta x \Delta r} \iint_{A_{i,j}} S(U)\, dx\, dr
\end{aligned}
\tag{17}
$$

where

$$
\tilde{U}_{i+1/2,j} = \bar{U}_{i,j}(x_{i+1/2}, r_j) \qquad \hat{U}_{i+1/2,j} = \bar{U}_{i+1,j}(x_{i+1/2}, r_j)
$$

and $\tilde{U}_{i,j+1/2}$ and $\hat{U}_{i,j+1/2}$ are defined similarly. Equation (17) has second-order accuracy in the smooth flow region.

Until now, the KFVS method with the combination of initial data reconstruction has been presented for the discretization of convective fluxes. For the diffusion terms, a central difference scheme is commonly used for the discretization of diffusive fluxes. For example, the derivatives in $r_j \tilde{E}_{i+1/2,j}$ are approximated by

$$
r_j(\tau_{xx})_{i+1/2,j} \approx r_j(2\mu + \tilde{\mu})_{i+1/2,j} \frac{1}{\Delta x}(u_{i+1,j} - u_{i,j}) + \tilde{\mu}_{i+1/2,j}
$$

$$
\times \left[\frac{1}{2}(v_{i+1,j} + v_{i,j}) + \frac{r_j}{4\Delta r}(v_{i+1,j+1} - v_{i+1,j-1} + v_{i,j+1} - v_{i,j-1}) \right]
$$

$$
r_j(\tau_{xr})_{i+1/2,j} \approx r_j\mu_{i+1/2,j} \left[\frac{1}{\Delta x}(v_{i+1,j} - v_{i,j}) + \frac{1}{4\Delta r}(u_{i+1,j+1} - u_{i+1,j-1} + u_{i,j+1} - u_{i,j-1}) \right]
$$

$$
r_j\left(k\frac{\partial T}{\partial x} \right)_{i+1/2,j} \approx k_{i+1/2,j}\frac{r_j}{\Delta x}(T_{i+1,j} - T_{i,j})
\tag{18}
$$

Time Discretizations

In the previous section we presented numerical approximation for the convective and difusive terms. To keep the second-order accuracy of the scheme, a second-order method must be used for the sorce terms. We now turn to the temporal discretization of Eq. (17). Denoting the right-hand side of Eq. (17) as $L(U)$ and omitting the spatial indices, Eq. (17) can be written as

$$
\frac{dU}{dt} = L(U)
\tag{19}
$$

The simplest single-step method for solving Eq. (19) is the explicit Euler method. However, there is usually a step size constraint associated with the convection and diffusive terms if the explicit Euler method is used. To overcome these difficulties, we use a third-order Runge–Kutta method [22] for the time discretization.

To advance the value of U from time level n to $n+1$ in Eq. (19) by the third-order Runge–Kutta method, we have

$$
\begin{aligned}
U^{(0)} &= U^n \\
U^{(1)} &= U^{(0)} + \Delta t L(U^{(0)}) \\
U^{(2)} &= \tfrac{3}{4} U^{(0)} + \tfrac{1}{4}(U^{(1)} + \Delta t L(U^{(1)})) \\
U^{(3)} &= \tfrac{1}{3} U^{(0)} + \tfrac{2}{3}(U^{(2)} + \Delta t L(U^{(2)})) \\
U^{n+1} &= U^{(3)}
\end{aligned}
\tag{20}
$$

NUMERICAL STUDY OF RESONANT OSCILLATIONS IN A TUBE

We now study the compressible flow oscillating inside a closed tube with a piston oscillating at the left end ($x = 0$) having the velocity $u = l\omega \cos(\omega t)$. Extensive computations using the above numerical method were carried out for the study of gas oscillations in a closed tube. The tube has a total length of $L = 1.7018$ m with the radius of $R_0 = 2.412 \times 10^{-2}$ m. The tube is filled with air under normal circumstances ($T_0 = 291.785$ K, $p_0 = 101325$ Pa). These parameters were used in a previous article by Saenger and Hudson [1]. The sound speed corresponding to the pressure and density of the air is $a_0 = 332.5317$. Therefore, the first resonant frequency of the tube becomes $f_r = \omega/2\pi = a_0/2L = 100.6$ Hz. The piston (at the end of the tube) has an oscillatory amplitude of $l = 3.175 \times 10^{-3}$ m [1]. The computational domain was divided into 160×40 grid points with equal cell size $\Delta x = 1.063625 \times 10^{-2}$ m and $\Delta r = 6.0325 \times 10^{-4}$ m. A schematic description of
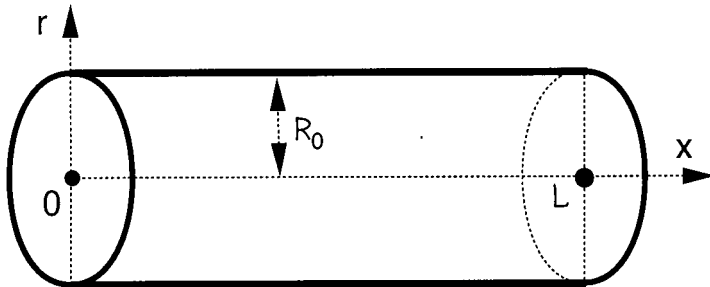

Figure 2. Schematic description of the tube and the coordinates.

the tube is given in Figure 2. In the following computations, the time step size Δt is determined by the Courant–Friedriche, Levy (CFL) condition

$$\Delta t \leq \frac{C_{CFL} \min\{\Delta x, \Delta r\}}{\max_U \{|u| + |v| + \sqrt{\gamma p / p}\}}$$

which comes from the explicit discretization of the convective terms, and C_{CFL} denotes CFL constant and is taken as 0.4.

No-slip boundary conditions for the fluid velocity are imposed at all solid walls. Both adiabatic wall and isothermal wall boundary conditions are considered. At the symmetry axis $(r = 0)$, the flow conditions $v = 0$ and $\partial \rho / \partial r = \partial u / \partial r = \partial p / \partial r = 0$ are imposed. Figures 3–10 show the numerical results for the case with an adiabatic wall with the piston oscillating at a resonant frequency of 100.6 Hz and two frequencies departing or far away from the resonant frequency, respectively, while Figures 11 and 12 show the results for the case of an isothermal wall. As is shown in these figures, the strength of the shock wave at the resonant frequency is weak. Because the strength of the shock wave is stronger in the case of the adiabatic all, we shall focus our discusson on this case.
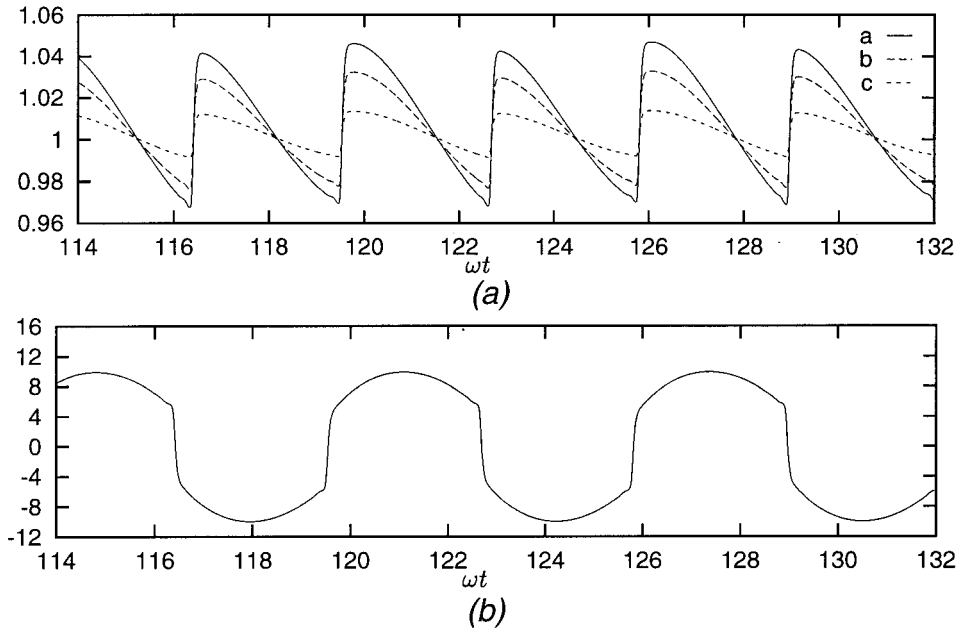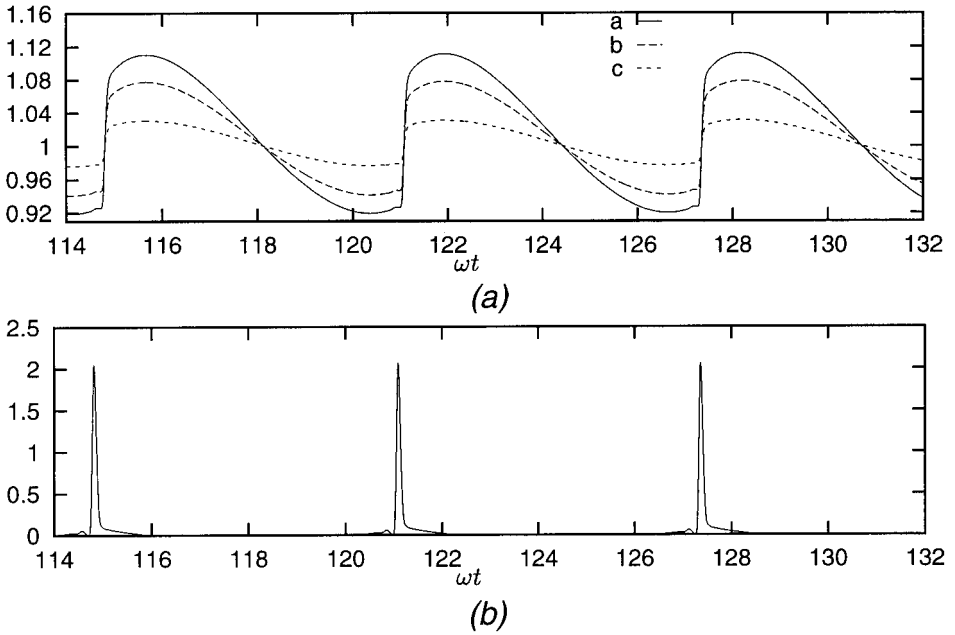

Figure 3. (*a*) Temporal variations of pressure, density, and temperature near the middle of the tube (at $x/L = 0.496875$ and $r = 0$) with an adiabatic wall at resonant frequency (i.e., $f = f_r = 100.6$ Hz). (a: p/p_0, b: ρ/ρ_0, C: T/T_0.) (*b*) Temporal variations of axial velocity $u/l\omega$ near the middle of the tube (at $x/L = 0.496875$ and $r = 0$) with an adiabatic wall at resonant frequency (i.e., $f = f_r = 100.6$ Hz).

Figures 3a and 3b show the temporal variations of pressure, density, temperature, and axial velocity near the midpoint of the tube (at $x/L = 0.496875$) and at the center line of the tube ($r = 0$). It is noted that the temporal variations of pressure, density, and temperature are in phase with each other. The periodically sharp increase in pressure, density, and temperature shown in Figure 3a indicates the propagation of a weak shock wave. Figure 3b shows the axial velocity near the middle of the tube, which varies almost sinuoisdally in the positive and negative direction periodically. The numerical results shown in Figures 3a and 3b are very similar to those presented in Figure 1 of Betchov's paper [2].

Figures 4a and 4b show the corresponding temporal variations of pressure, density, temperature, and axial velocity near the piston ($x/L = 3.125 \times 10^{-3}$ and $r = 0$). A comparison of Figure 4a and Figure 3a shows that the period and amplitude of temporal variations of pressure, density, and temperature at a location near the piston, which are larger than those near the middle of the tube. At a small distance away from the piston, the temporal variations of axial velocity shown in Figure 4b are almost sinusoidally in phase with the piston movement. The weak shock wave is generated whenever there is a sudden increase in pressure and the axial velocity is suddenly changed from zero to a negative value, which forms a pulse-type shock wave.
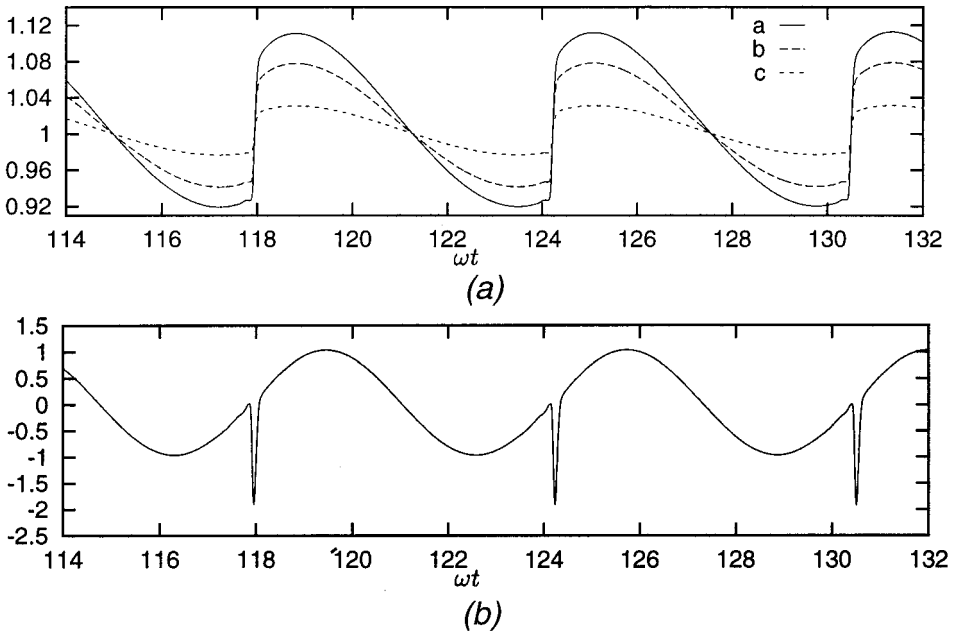
Figure 4. Temperoral variations of pressure, density, and temperature near the piston (at $x/L = 3.125 \times 10^{-3}$ and $r = 0$) with an adiabatic wall at resonant frequency (i.e., $f = f_r = 100.6$ Hz). (a: p/p_0, b: ρ/ρ_0, c: T/T_0.) (b) Temporal variations of axial velocity $u/l\omega$ near the piston (at $x/L = 3.125 \times 10^{-3}$ and $r = 0$) with an adiabatic wall at resonant frequency (i.e., $f = f_r = 100.6$ Hz).
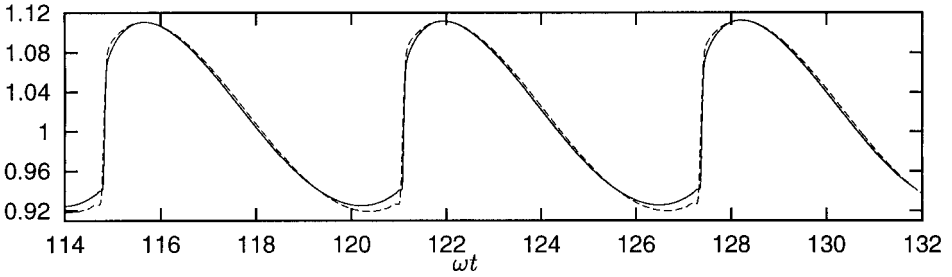
Figure 5. (*a*) Temporal variations of pressure density, and temperature near the closed end (at $x/L = 0.996875$ and $r = 0$) with an adiabatic wall at resonant frequency (i.e., $f = f_r = 100.6$ Hz). (a: p/p_0, b: ρ/ρ_0, c: T/T_0.) (*b*) Temporal variations of velocity $u/l\omega$ near the closed end (at $x/L = 0.996875$ and $r = 0$) with an adiabatic wall at resonant frequency (i.e., $f = f_r = 100.6$ Hz).

The corresponding temporal variations of pressure, density, temperature, and axial velocity near the closed end are shown in Figures 5*a* and 5*b*. A comparison of Figures 3*a*, 4*a*, and 5*a* shows that (1) the period and amplitude of temporal variatons of pressure, density, and temperature near the piston and the closed end are almost identical, and (2) the amplitudes of these oscillations are smallest near the middle of the tube. Figure 5*b* shows the temporal variation of axial velocity near the closed end (at $x/L = 0.996875$ and $r = 0$), which are small except during the occurrence of a shock wave. It is interesting to note that the axial velocity is always nonnegative near the closed end at $x/L = 1$ and the weak shock appears as a pulse-type axial velocity variation.

Figure 6 shows the mesh refinement study of the same problem, where solid and dashed lines denote pressure near the closed end as a function of time obtained with 160×40 and 320×80 mesh points, respectively. It is shown that there are only slight differences in pressure near the valley of the curve when a refined grid size was used. We also refer the readers to [20, 21] for detailed grid convergence analyses of the gas kinetic method.

Figure 7*a* gives axial velocity and temperature profiles at six different locations of x/L at $t = 0.486$ s. As shown in this figure, the maximum axial velocity occurs near the wall of the tube. Figure 7*b* shows that the temperature variations along the radial direction are small for this case with an adiabatic wall.

Figure 6. Mesh refinement study of pressure as a function of time near the closed end (at $x/L = 0.996875$) with an adiabatic wall at $f = 100.6$ Hz. Solid and dashed lines denote solutions on the fine and coarse grids, respectively.
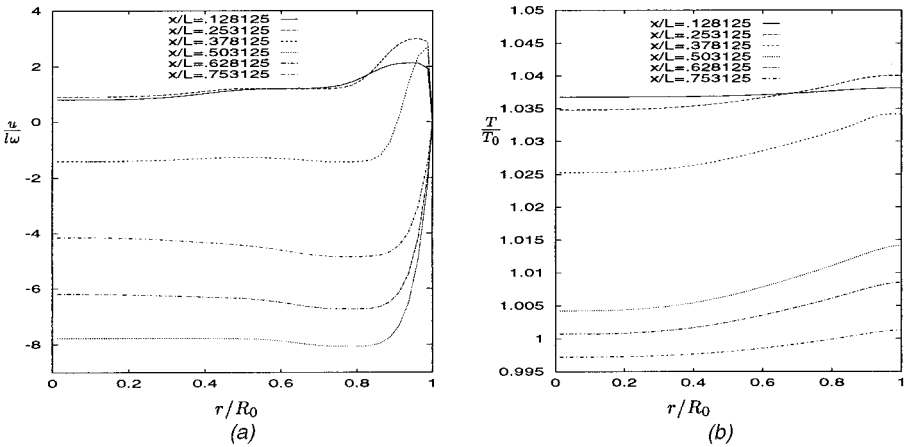

Figure 7. Axial velocity and temperature profiles with an adiabatic wall at $t = 0.486$ s at different locations x/L at resonant frequency of $f = f_r = 100.6$ Hz.

Figure 8 shows the distribution of the pressure, density, and temperature along the tube at two different times at $t_1 = 0.4023$ s and $t_2 = 0.4077$ s, while Figure 9 shows the corresponding axial velocity. Figure 9a indicates the axial velocity at $t = 0.4023$ s at which time the piston is moving to the left ($u(0, 0.4023) < 0$ in Figure 8) and the shock wave is moving from the closed end ($x = L$) to the piston ($x = 0$). Figure 9b indicates the axial velocity at $t = 0.4077$ s at which time the piston is moving to the right ($u(0, 0.4077) > 0$ in Figure 8) and the shock wave is moving to the right ($u(0, 0.4077) > 0$ in Figure 8) and the shock wave is moving toward the closed end.
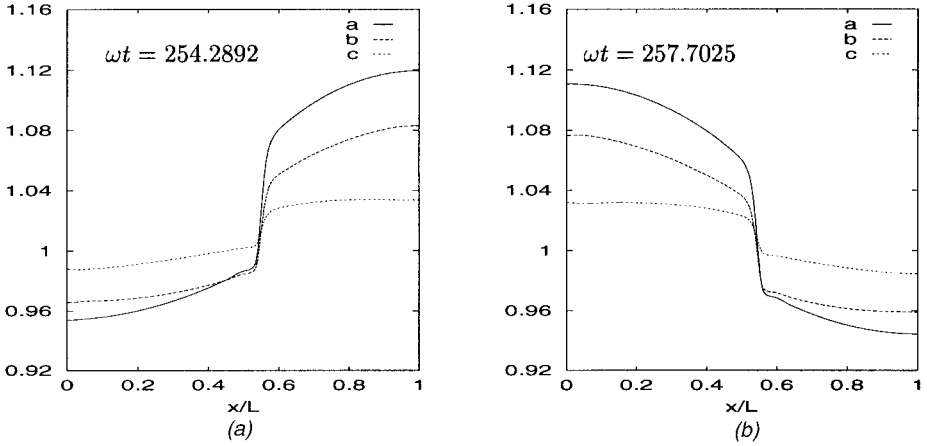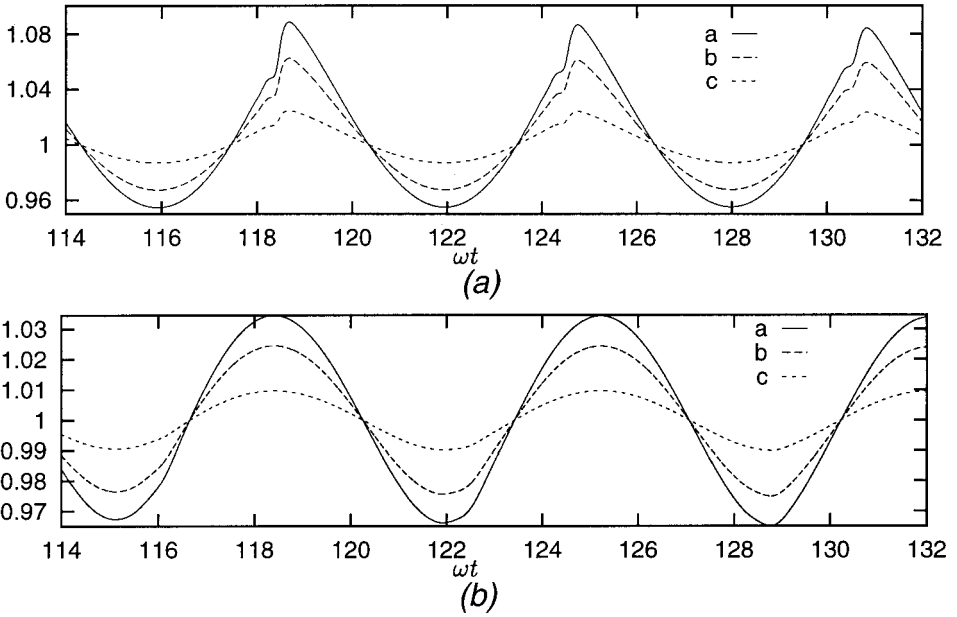
Figure 8. Axial variations of pressure, density, and temperature along center line ($r = 0$) at $\omega t = 254.2892$ (a) and $\omega t = 257.7025$ (b) with an adiabatic wall at resonant freqency of $f = f_r = 100.6$ Hz. (a: p/p_0, b: ρ/ρ_0, c: T/T_0).
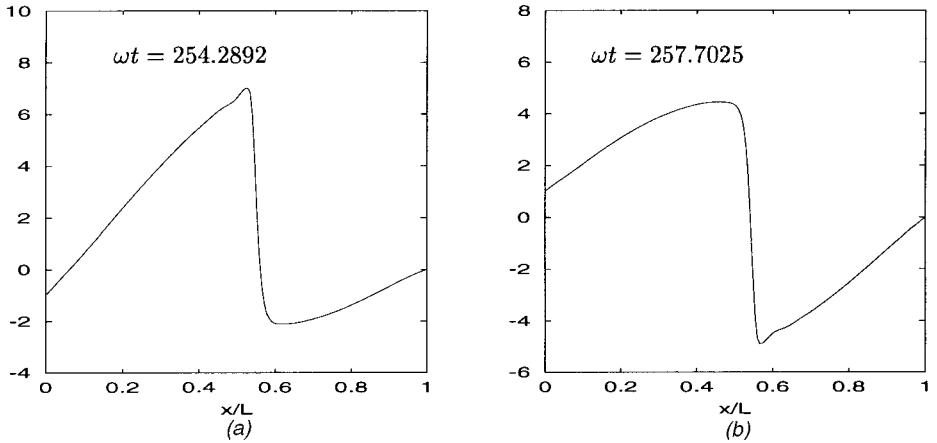

Figure 9. $u/l\omega$ vs. x/L at $\omega t = 254.2892$ (a) and $\omega t = 257.7025$ (b) with an adiabatic wall at resonant frequency of $f = f_r = 100.6$ Hz.

When the oscillating frequency ($f = 104.7$ Hz) of the piston departs from the resonant frequency ($f = 100.6$ Hz), the shock wave generated inside the tube becomes weaker as shown in Figure 10a. If the oscillation frequency ($f = 92.3$ Hz) is far away from the resonance frequency ($f = 100.6$ Hz), the piston only generates standing waves moving in the tube as shown in Figure 10b which does not have a shock wave.

Figure 10. (*a*) Temporal variations of pressure, density, and temperature near the closed end (at $x/L = 0.996875$) with an adiabatic wall at $f = 104.7$ Hz. (a: p/p_0, b: ρ/ρ_0, c: T/T_0). (*b*) Temporal variations of pressure, density, and temperature near the closed end (at $x/L = 0.996875$) with an adiabatic wall at $f = 92.3$ Hz. (a: p/p_0, b: ρ/ρ_0, c: T/T_0.)

The numerical results with an isothermal wall condition are shown in Figures 11 and 12. Similar wave structures are observed inside the tube even though the shock waves become much weaker in this case as compared with the adiabatic case. (See Figures 5*a* and 11*a*). This is because for the adiabatic case there is no heat loss from the fluid to the wall, whereas for the isothermal wall there is heat transfer from the flow to the wall at certain locations along the wall. At the resonant frequency of 100.6 Hz, the captured shock waves can be clearly observed. Figure 11*b* shows the radial distribution of the axial velocity (left) and temperature profiles (right) at $t = 0.391$ s at different locations at resonant frequency. It is shown that the axial velocity (left figure) is positive in most locations away from the closed end, which means that the gas at most locations at this instant is moving from the piston to the closed end. Near the closed end, the axial velocity is negative, which implies that the wave is reflected at the instant. Radial temperature gradients near the wall are negative near the piston and positive near the closed end, which indicate that heat is transferred from the gas to the wall near the piston and heat is transfered from the wall to the gas near the closed end. (See Figure 11*a*.) However, at $f = 97.7$ Hz, which is away from the resonant frequency ($f = 100.6$ Hz), the weak shock waves as shown in Figure 12*a* are much more easily spread out in comparison with the adiabatic case. Figure 12*b* shows that the corresponding axial velocity and temperature distributions at different locations x/L at $f = 99.7$ Hz, which have similar behavior to Figure 11*b*.
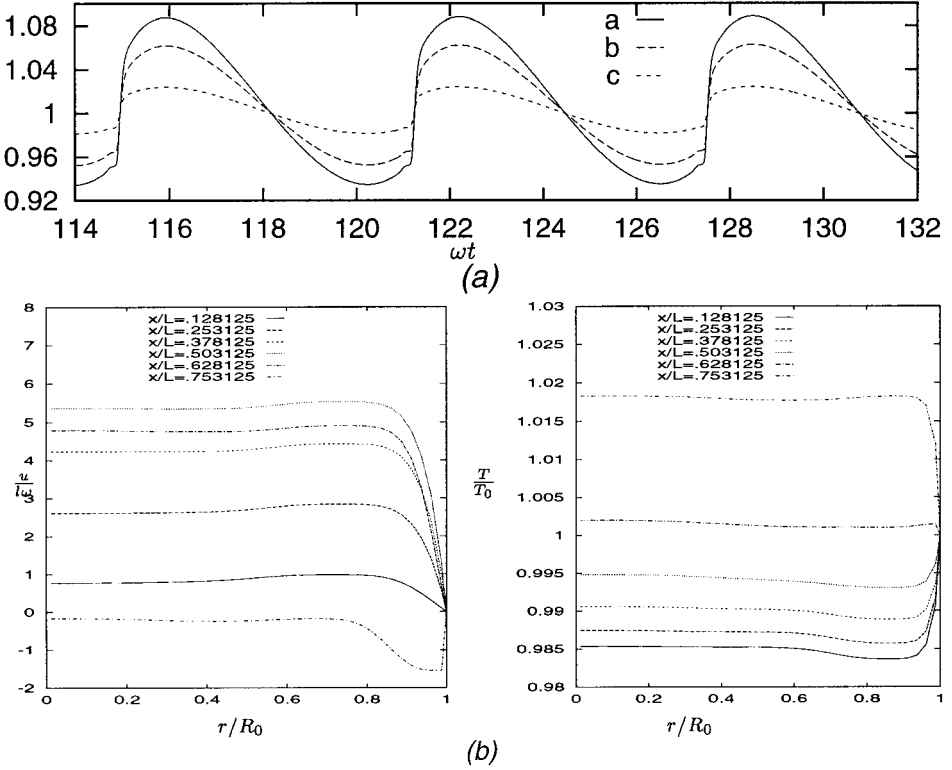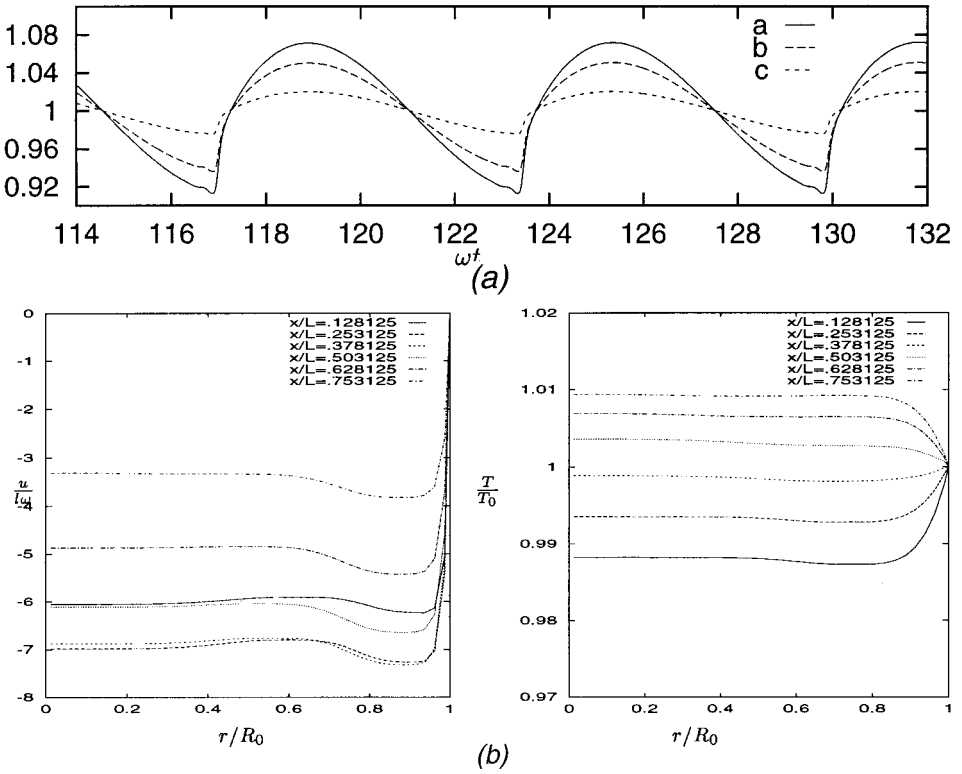
Figure 11. (*a*) Temporal variations of pressure, density, and temperature near the closed end (at $x/L = 0.996875$) with an isothermal wall at resonant frequency of $f = f_r = 100.6$ Hz. (a: p/p_0, b: ρ/ρ_0, c: T/T_0.) (*b*) Axial velocity and temperature profiles at $t = 0.391$ s and at different locations x/L with an isothermal wall at resonant frequency of $f = f_r = 100.6$ Hz.

DISCUSSION AND CONCLUSION

In this article we have presented a gas-kinetic scheme to simulate two-dimensional resonant gas oscillations in a tube. The MUSCL-type KFVS methods for convective terms and a third-order Runge–Kutta time discretization were used to approximate numerically the time-dependent, axisymmetric, compressible Navier–Stokes equations.

The oscillatory motion is generated by a piston at one end and reflected by another closed end. The dependence of the flow distribution on the different oscillating frequencies and wall boundary conditions are presented. At the resonant frequency and slightly off-resonance frequencies, weak shock waves propagating inside the tube are captured very well, even though the oscillation amplitude is small and the flow Mach number is very low. These results are consistent with those from both experimental observation and previous theoretical anlyses. The results also show the interesting phenomena of a pulse-type shock wave, which appeared in the axial velocity near the piston and near the closed end.

Figure 12. (*a*) Temporal variations of pressure density, and temperature near the closed end (at $x/L = 0.996875$) with an isothermal wall at a frequency of $f = 97.7$ Hz. (a: p/r_0, b: ρ/ρ_0, c: T/T_0.) (*b*) Axial velocity and temperature profiles at $t = 0.394$ s and at different locations x/L with an isothermal wall at a frequency of $f = 97.7$ Hz.

REFERENCES

1. R. A. Saenger and G. E. Hudson, Periodic Shock Waves in Resonating Gas Columns, *J. Accoust. Soc. Am.* vol. 32, pp. 961–971, 1960.

2. R. Betchov, Nonlinear Oscillations of a Column of Gas, *Phys. Fluid*, vol. 1, pp. 205–212, 1958.

3. W. Chester, Resonant Oscillations in Closed Tubes, *J. Fluid Mech.*, vol. 18, pp. 44–64, 1964.

4. P. Merkli and H. Thomann, Thermoacoustic Effects in Resonance Tube, *J. Fluid Mech.*, vol. 70, pp. 161–177, 1975.

5. A. Gopinath, N. L. Tait, and S. L. Garrett, Thermoacoustic Streaming in a Resonant Channel: The Time Averaged Temperature Distribution, *J. Acoust. Soc. Am.*, vol. 103, pp. 1388–1405, 1998.

6. L. Bauwens, Oscillating Flow of a Heat-Conducting Fluid in a Narrow Tube, *J. Fluid Mech.*, vol. 324, pp. 135–161, 1996.

7. A. Goldshtein, P. Vainshtein, M. Fichman, and C. Gutfinger, Resonance Gas Oscillations in Closed Tubes, *J. Fluid Mech*, vol. 322, pp. 147–163, 1996.

8. C. P. Lee and T. G. Wang, Nonlinear Resonance and Viscous Disspation in an Acoustic Chamber, *J. Acous. Soc. Am.*, vol. 92, pp. 2195–2206, 1992.

9. L. Elvira-Segura and E. Sarabia, Numerical and Experimental Study of Finite-Amplitude Standing Waves in a Tube at High Sonic Frequencies, *J. Acous. Soc. Am.*, vol. 104, pp. 708–714, 1998.

10. T. Schneider, N. Botta, K. J. Geratz, and R. Klein, Extension of Finite Volume Compressible Flow Solvers to Multi-Dimensional, Variable Density Zero Mach Number Flows, *J. Comput. Phys.*, vol. 155, pp. 248–286, 1999.

11. A. Harten, High-Resolution Schemes for Hyperbolic Conservation Laws, *J. Comput. Phys.*, vol. 49, pp. 357–393, 1983.

12. A. Harten, B. Engquist, S. Osher, and S. R. Chakravarthy, Uniformly High-Order Accurate Non-Oscillatory Schemes III, *J. Comput. Phys.*, vol. 71, pp. 231–303, 1987.

13. B. van Leer, Towards the Ultimate Conservative Difference Scheme V. A Second-Order Sequel to Godunov's Method, *J. Comput. Phys.*, vol. 32, pp. 101–136, 1979.

14. D. Drikakis and F. Durst, Investigation of Flux Formulae in Transonic Shock Wave/Turbulent Boundary Layer Interaction, *Int. J. Numer. Math. Fluids*, vol. 18, pp. 385–413, 1994.

15. H. C. Ye, G. H. Klopfer, and J. L. Montagne, High Resolution Shock Capturing Schemes for Inviscid and Viscous Hypersonic Flows, *J. Comput. Phys.*, vol. 88, pp. 31–61, 1990.

16. R. J. LeVeque, *Numerical Methods for Conservation Laws*, Birkhäuser-Verlag, 1990.

17. E. F. Toro, *Riemann Solvers and Numerical Methods for Fluid Dynamics, A Practical Introduction*, 2nd ed., Springer, Berlin, New York, 1999.

18. D. I. Pullin, Direct Simulation Methods for Compressible Inviscid Ideal Gas Flow, *J. Comput. Phys.*, vol. 34, pp. 231–244, 1980.

19. J. L. Steger and R. F. Warming, Flux-Vector Splitting of the Inviscid Gas-Dynamic Equations with Applicatons to Finite Difference Schemes, *J. Comput. Phys.*, vol. 40, pp. 263–293, 1981.

20. K. Xu, L. Martinelli, and A. Jameson, Gas-Kinetic Volume Methods, Flux-Vector Splitting and Artificial Diffusion, *J. Comput. Phys.*, vol. 120, pp. 48–65, 1995.

21. H. Z. Tang and H. M. Wu, Kinetic Flux Vector Splitting for Radiation Hydrodynamic Equations, *Computers & Fluids*, vol. 29, pp. 917–933, 2000.

22. C. W. Shu, Total-Variation-Diminishing Time Discretizations, *SIAM J. Sci. Statist. Comput.*, vol. 9, pp. 1073–1084, 1988.